Valley-hybridized gate-tunable 1D exciton confinement in $MoSe_2$

DOI:
10.1021/acsnano.4c04786

Document Version
Accepted author manuscript

Valley-hybridized gate-tunable 1D exciton confinement in $MoSe_2$

Maximilian Heithoff[1], Álvaro Moreno[1], Iacopo Torre[1], Matthew S. G. Feuer[2], Carola M. Purser[2,3], Gian Marcello Andolina[1], Giuseppe Calajo[1,4], Kenji Watanabe[5], Takashi Taniguchi[6], Dhiren M. Kara[2], Patrick Hays[7], Seth Ariel Tongay[7], Vladimir I. Fal'ko[8,9,10], Darrick Chang[1,11], Mete Atatüre[2], Antoine Reserbat-Plantey[1,12,], Frank H.L. Koppens[1,11,*]*

[1]ICFO – Institut de Ciencies Fotoniques, Castelldefels (Barcelona), 08860, Spain

[2]Cavendish Laboratory, University of Cambridge, JJ Thomson Avenue, Cambridge, CB3 0HE, UK

[3]Cambridge Graphene Centre, University of Cambridge, CB3 0FA, UK

[4]Instituto Nazionale di Fisica Nucleare (INFN), Sezione di Padova, Padova, I-35131, Italy

[5]Research Center for Electronic and Optical Materials, National Institute for Materials Science, Tsukuba, 305-0044, Japan

[6] Research Center for Materials Nanoarchitectonics, National Institute for Materials Science, Tsukuba, 305-0044, Japan

[7]School for Engineering of Matter, Transport and Energy, Arizona State University, Tempe, AZ 85287, United States

[8]National Graphene Institute, Manchester, M13 9PL, UK

[9]Department of Physics and Astronomy, University of Manchester, UK

[10]Henry Royce Institute for Advanced Materials, Manchester, UK

[11]ICREA, Barcelona, Spain

[12]Université Côté d'Azur, CNRS, CRHEA. Valbonne, Sophia-Antipolis, 06560, France

Keywords: 2D semiconductors, quantum photonics, 1D excitons, van der Waals heterostructures, Transition Metal Dichalcogenides

Abstract

Controlling excitons at the nanoscale in semiconductor materials represents a formidable challenge in quantum photonics and optoelectronics fields. Monolayers of transition metal dichalcogenides (TMDs) offer inherent two-dimensional confinement and possess significant exciton binding energies, making them promising candidates for achieving electric-field-based confinement of excitons without dissociation. Exploiting the valley degree of freedom associated with these confined states further broadens the prospects for exciton engineering. Here, we show electric control of light polarization emitted from one-dimensional (1D) quantum-confined states in $MoSe_2$. Building on previous reports of tunable trapping potentials and linearly polarized emission, we extend this understanding by demonstrating how non-uniform in-plane electric fields enable in-situ control of these effects and highlight the role of gate-tunable valley hybridization in these localized states. Their polarization is entirely engineered through either the 1D confinement potential's geometry or an out-of-plane magnetic field. Controlling non-uniform in-plane electric fields in TMDs enables control of

the energy (up to five times its linewidth), polarization state (from circular to linear), and position of 1D confined excitonic states (5 $\mathrm{nm.V^{-1}}$).

INTRODUCTION

The manipulation of the dimensionality of a physical system has proven to be highly effective for controlling the behavior of quasiparticles. Achieving this control holds excellent potential for unlocking strong exciton-exciton interaction regimes[1,2], enabling exciton-based logic operations[3], exploring exotic quantum phases of matter[4,5], facilitating deterministic positioning and tuning of quantum emitters[6,7], and designing advanced optoelectronic devices[8,9]. Prominent examples include the discovery of the quantum Hall effect, Luttinger liquids[10], electron quantum dots[11], hydrodynamic phonon transport[12], and van der Waals heterostructures. Among various quasiparticles, engineering the dimensionality of excitonic potentials plays a pivotal role in designing efficient exciton dissociation in photodetectors[8] and establishing the foundations for quantum technologies centered around localized excitons, such as single photon sources[6,7], qubit arrays[13], and exciton routers[3].

Approaches for manipulating excitons in two-dimensional (2D) semiconducting crystals can be broadly categorized into three primary classes. The first category involves the local trapping of excitons in zero-dimensional systems, thereby enabling single photon emission[14]. Deterministic methods employed in this approach encompass the utilization of nano-pillars[6,7] to induce local strain, defect implantation through techniques like He-FIB[15], and, more recently, utilizing moiré potentials[1,13,16]. These endeavors hold significant promise for applications in quantum technologies[17], including quantum key distribution, photon storage exploiting collective effects in arrays of quantum emitters, multiplexing indistinguishable photon sources, and solid-state quantum simulators. However, this approach currently lacks in situ control over the energies and positioning of quantum emitters, which hampers efficient manipulation of ensembles of such emitters.

The second avenue involves leveraging interlayer exciton states in van der Waals heterostructures similar to initial studies in double quantum well[18]. In this context, an out-of-plane electric field can effectively couple to the dipole of the interlayer exciton, yielding significant achievements such as quantum-confined Stark tuning[19,20], electrical control of exciton dynamics[21], and the realization of exciton-based transistors[3] or routers[22]. However, several challenges must be addressed, such as the fabrication of high-quality heterostructure devices, intricate mesoscopic reconstruction of the heterointerface[23], and the relatively slow recombination rates observed in indirect interlayer excitons, limiting the photoluminescence brightness.

The third approach encompasses directly manipulating the dielectric[24] or electrostatic[25–27] environment of a neutral intra-layer exciton. Initial efforts in this direction involved the creation of non-homogeneous dielectric environments by partially covering a TMD with graphene or hexagonal boron nitride (hBN)[24]. Such in-plane heterostructures lead to a significant alteration of electronic properties at the interface edge[24,25]. The precise nature of 1D excitonic states at these edges has been further explored in systems characterized by 1D strain gradients[28] or using carbon nanotubes grids[29]. Furthermore, by harnessing the substantial in-plane electric field at the boundary between two ferroelectric domains[30], exciton drift, and dissociation effects have been observed in monolayer TMD when deposited atop such domains. There has been considerable momentum in optoelectronics towards designing efficient photodetectors by engineering ultra-sharp PN junctions using split gates[8,9]. While these structures promote exciton dissociation, the large excitonic binding energy provides an opportunity for exciton confinement through electrostatic gates. Recently, an important breakthrough[25] and follow-up works[26,27] have demonstrated 1D and 0D confinement of intra-layer excitons by fabricating lateral P-i-N junctions with dimensions as small as 10 nm in $MoSe_2$. An alternative approach[31] is using the AFM tip as a scanning gate to locally confine

exciton complexes. These studies have suggested ways for electrical control of exciton wavefunctions, down to the 0D quantum dot limit[26]. Several aspects of the physics underlying these phenomena are still being discussed, such as the exact nature of these localized excitonic states, their dependence on magnetic field, or the appearance of 1D polarized states, which we are addressing here.

RESULTS AND DISCUSSION

Intra-layer exciton confinement in electrostatic traps encounters a fundamental challenge posed by an in-plane electric field, which can induce the dissociation of excitons. In our study, we addressed this issue by leveraging the substantial binding energy of intra-layer neutral excitons in $MoSe_2$, similar to previous works on 1D and 0D exciton confinement in TMDs[25–27]. Specifically, we apply an inhomogeneous electric field on a nanoscale region to achieve center-of-mass localization and observe discrete quantized states. Furthermore, we investigate the possibilities of engineering the trap's geometry to establish an artificial 1D exciton channel. The resulting confinement potential exhibits significant localization, with exciton confinement below 5 nm and electrically tunable positioning in a few tens of nanometers away from a designer top gate electrode similar to previous reports[25,27]. In addition to replicating these findings, we demonstrate that the localized states within this setup are linearly polarized, and we explain this with a model that incorporates significant inter-valley exchange interaction. The hybridization between valleys can be further tuned with an out-of-plane magnetic field that leads to purely circularly emitted light from the 1D-localized exciton states. Lastly, we provide an understanding of the interplay between the out-of-plane magnetic field and the in-plane electric field, which helps clarify the underlying mechanisms governing the formation of such a 1D confinement potential.

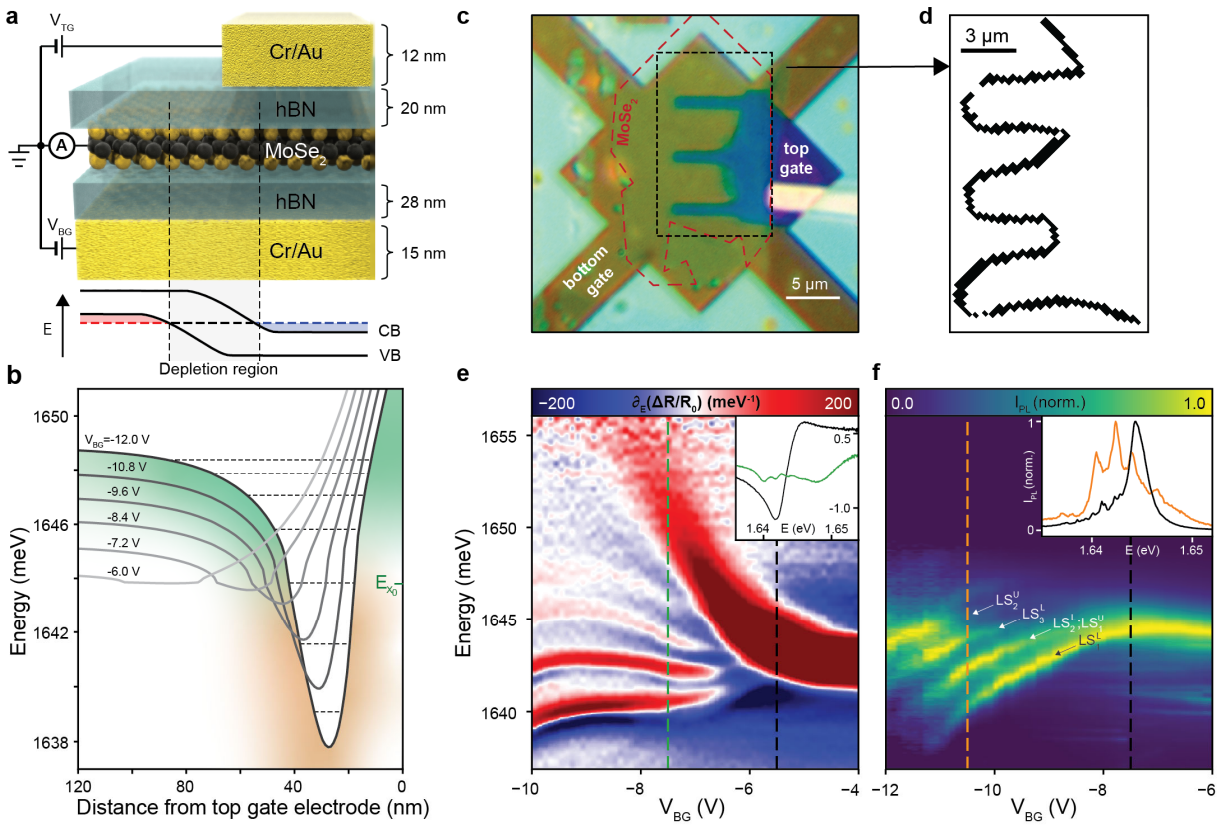
a
V_{TG}
Cr/Au
12 nm
hBN
20 nm
$MoSe_2$
hBN
28 nm
V_{BG}
Cr/Au
15 nm
A
E
CB
VB
Depletion region
b
V_{BG}=-12.0 V
-10.8 V
-9.6 V
-8.4 V
-7.2 V
-6.0 V
E_{X_0}
Energy (meV)
1650
1646
1642
1638
120
80
40
0
Distance from top gate electrode (nm)
c
$MoSe_2$
top gate
bottom gate
5 µm
d
3 µm
e
−200
$\partial_E(\Delta R/R_0)$ (meV^{-1})
200
0.5
-1.0
1.64
E (eV)
1.65
Energy (meV)
1655
1650
1645
1640
−10
−8
−6
−4
V_{BG} (V)
f
0.0
I_{PL} (norm.)
1.0
1
0
I_{PL} (norm.)
1.64
E (eV)
1.65
LS_2^U
LS_2^L
LS_2^L;LS_2^U
LS_1^L
−12
−10
−8
−6
V_{BG} (V)

Figure 1: Gate-controlled 1D-excitonic potential in $MoSe_2$ monolayer. a: Sketch of the device. This geometry unlocks high gradients in charge carrier densities and in-plane electric field at the top gate edge, where combination of Stark and interaction effects generates a narrow 1D-potential channel. P-i-N configuration around the top electrode is represented by the VB and CB edge diagram. **b**: Simulated trapping potential using Eq. 1 as a function of the in-plane distance from the top gate electrode edge for several values of V_{BG}. The green (orange) colour indicates the potential being mostly governed by interaction shift (Stark shift). Calculated localized states energy are shown (dashed lines) for $V_{BG} = -12$ V as well as the neutral exciton energy E_{X_0} for comparison. **c:** Optical microscope image of the device. **d:** Modulus of the spatial gradient of differential reflectance taken at E_{X_0} defined by $\boldsymbol{\nabla}_{x,y}(\Delta R/R_0)\,|_{E_{X_0}}$. The objective is scanned in (x, y) plane and $V_{BG} = -10\ V$. This quantity depicts the spatial onset of the 1D potential channel formed around the top gate electrode. **e:** Derivative of differential reflectance spectrum $\partial_E(\Delta R/R_0)$ versus V_{BG}. Single differential reflectance spectra taken at $V_{BG} = [-7.5,\ -5.5\ V]$ and represented by the vertical dashed lines (cf. respective colours in inset). **f:** Dependence of photoluminescence spectra with respect to V_{BG}. Each spectrum is normalized by its maximum. Inset shows two spectra taken at $V_{BG} = [-10.5, -7.5\ V]$. In **e,f** light is collected at the edge of the top gate electrode. All measurements and simulations are performed at $V_{TG} = 10\ V$ and $T = 3\ K$.

The device consists of an hBN-encapsulated $MoSe_2$ monolayer placed in between a global bottom-gate and a local fingered top-gate (see Fig. 1a-b). Among other materials, $MoSe_2$ has the advantage of lesser hybridization with dark states at low-temperature. The device is essentially the same geometry as in previous reports on electric control of 1D excitons[25,27]. The

$MoSe_2$ monolayer covers most of the bottom-gate electrode, while top-gate fingers are 1 µm wide (see Fig. 1c). The bottom and top-gate potentials – V_{BG} and V_{TG}, respectively – can be independently controlled while $MoSe_2$ is grounded. Contact to $MoSe_2$ is made by a gold electrode capped with thin graphite membrane (Supplementary Note 1). This asymmetric double gate geometry generates strong spatial inhomogeneities of charge carrier density n within the $MoSe_2$ monolayer (see Fig. 1a-b). For instance, a negative bottom-gate potential ($V_{BG} = -10$ V) leads to an excess of holes in the $MoSe_2$. By sufficiently increasing the top-gate potential ($V_{TG} = 10$ V), negative charge carriers accumulate in the $MoSe_2$ area below the top-gate electrode. Such a gate combination creates a narrow PN-junction, with a depletion region's width governed by the large capacitive coupling between the top-gate and $MoSe_2$, facilitated by the thin top hBN spacer ($h_{hBN} \sim 20$ nm)[25]. Only in this depletion region can the monolayer be efficiently penetrated by a large in-plane component of the electric field $\mathcal{E}$ generated at the top-gate edge, further enhanced by the small distance between the $MoSe_2$ and the top-gate electrode. Along the edge of the top-gate electrode, we can define a total exciton potential:

$$V_{tot} = -\frac{1}{2}\alpha\mathcal{E}^2 + \beta|n|, \qquad \text{Eq. 1}$$

with two contributions: i) within the narrow depletion region, a quadratic Stark potential originating from the large in-plane electric field $\mathcal{E}$ with polarizability α, and ii) outside the depletion region, a repulsive interaction with scaling factor β when excitons get dressed into polarons by the sea of free charge carriers[32,33]. This resulting 1D potential channel will lead to observable quantum-confined excitonic states if the energy splitting ΔE_n between states is larger than their linewidth. We reach that regime at cryogenic temperatures ($T = 3$ K), where encapsulated $MoSe_2$ usually exhibits narrow excitonic emission linewidths[34] $\Gamma \sim 1$ meV. The exact position of the center-of-mass of the confined excitons can be electrically tuned ($\sim 5\ \mathrm{nm.V^{-1}}$) with nanometer-scale precision (Supplementary Note 2), which is an interesting

flexible feature for excitonic confinement compared to strategies based on rigid and fixed positioning[6,7,14,28].

To monitor the emergence of this confinement potential, we perform low-temperature reflectance contrast (RC) and photoluminescence (PL) measurements as a function of gate voltages V_{BG}, V_{TG} (see Fig. 1e-f). By setting the top-gate voltage at a high positive value ($V_{TG} = 10$ V), we can increase locally the density of negative charge carriers in $MoSe_2$ located below the top-gate electrode. When sweeping the bottom-gate voltage towards negative values, the hole density in $MoSe_2$ increases in the area uncovered by the top-gate electrode. Consequently, V_{BG} acts as a knob to establish a confinement potential at the top-gate electrode edge (opposite polarity is shown in Supplementary Note 3). In Fig. 1e, we display RC as a function of V_{BG} and plot its spectral differential for clarity. At $V_{BG} > -6$ V, we observe a stable and gate-voltage independent 1s neutral exciton line. There is a drastic behavior change around $V_{BG}^{*} = -6$ V: the neutral exciton strongly blueshifts, indicating an increasing p-doping, and four narrow additional lines appear with similar linewidth $\Gamma_{LS} \sim 1$ meV. The emergence of these additional lines in the spectrum can be attributed to localized states (temporarily referred to as LS_{a-d}) that are trapped within the 1D confinement potential created around the top-gate electrode. The spacing between consecutive states reaches a maximum value of $\Delta E_n \sim 2.4$ meV. This value suggests tight center-of-mass confinement for the excitons with a typical spatial extent – within the harmonic oscillator approximation – defined by $\ell = \sqrt{\hbar/(m_X \omega)} \sim 5$ nm, with $m_X \sim 1.3\, m_e$ and $\hbar\omega = \Delta E_n$ being the energy splitting between localized states. The presence of redshifted and blueshifted localized states compared to the neutral exciton energy E_{X^0} suggests the combined influence of both Stark and interaction-induced energy shifts on the formation of the trapping potential, as previously established in similar geometries[25–27].

To further characterize these spectral features, we perform additional micro-photoluminescence (μ-PL) measurements (Fig. 1f) showing a similar fan of narrow lines for large negative bottom-gate voltages. The PL intensity of the neutral exciton line vanishes for $V_{BG} < V_{BG}^{*}$, as introducing additional charge carriers offers a decay pathway towards the energetically more favorable attractive polaron state[35]. For the localized states with a thermalized exciton population, we expect the lowest energy state – LS_1^L – to feature the largest PL intensity. Please refer to Fig. 3 and Eq. 2 for clarification on labeling the localized states. Interestingly, we observe a different behavior as the most intense peak is not always LS_1^L. For instance, the intensity of LS_1^L is the highest for $V_{BG} > -10V$ while the third line LS_3^L dominates around $V_{BG} \sim -11V$. This is due to exciton population decay channels associated with exciton dissociation and polaron-exciton interactions[36]. Specifically, lower energy states wavefunctions show a larger overlap with the in-plane electric field $\mathcal{E}$, which eventually becomes sufficiently strong to induce exciton dissociation. Higher energy states rather overlap with the sea of charge carriers in the doped regions, opening up a decay channel into attractive polaronic states.

Significantly, all the mechanisms described here strongly depend on the spatial position, as the confinement potential only appears near the top-gate electrode (Supplementary Note 4). To visualize this confinement potential, we record reflectance spectra for each point of the device and extract the spatial gradient of $\Delta R/R_0$ at the neutral exciton energy E_{X_0}, showing the spatial extent of the confinement potential (see Fig. 1d). Interestingly, the confinement potential strictly follows the edge of the top-gate electrode without discontinuities, with a very abrupt change in the spectral response when the laser spot is scanned toward the top gate electrode edge. (Supplementary Note 4). In the following, we investigate the origin and geometry of this potential by performing polarization-resolved measurements.

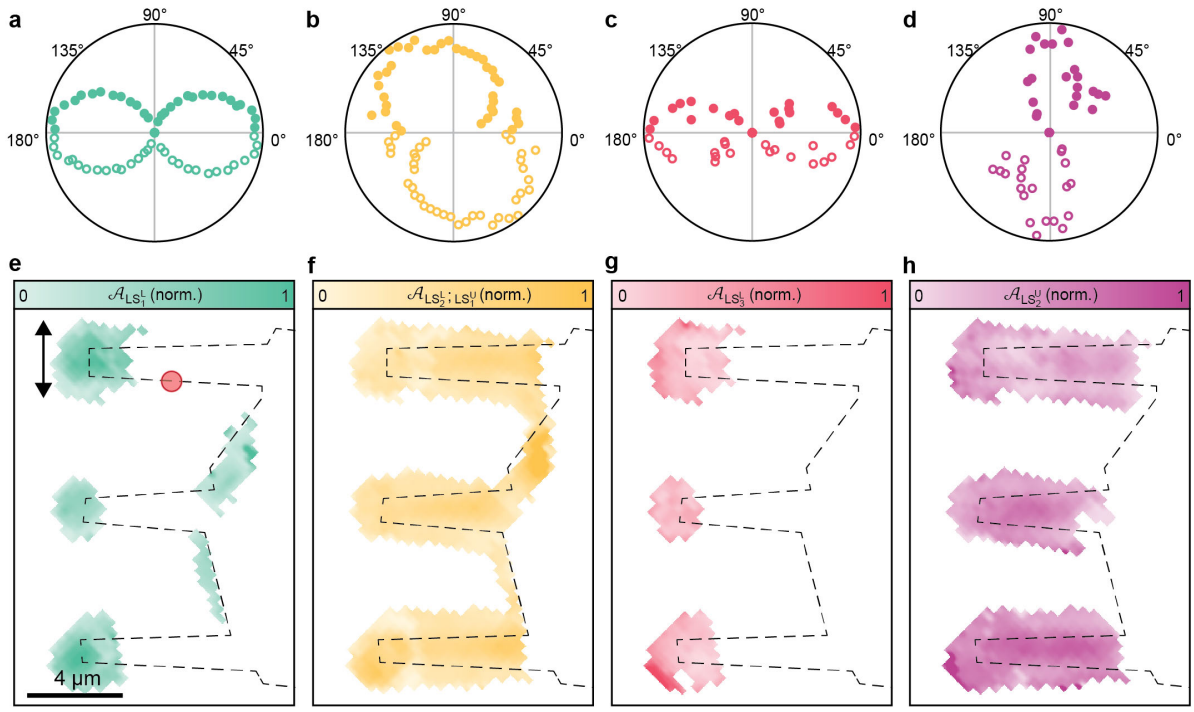

Figure 2: Polarized 1D-localized states in $MoSe_2$. Fitted weight $\mathcal{A}$ of localized states' spectral components in RC as a function of the excitation polarization (**a-d**) and laser spot position (**e–h**). In all cases, both excitation and collection polarizations are colinear. In **a-d** the laser is focused at the edge of the top gate electrode (see red spot in panel **e**), while in **e–h** the excitation polarization is fixed is set at 90° (see arrow in panel **e**). For convenience in **a-d**, angle 0° corresponds to the longer edge of the top gate electrode fingers, with data from 0° to 180° mirrored. All measurements were taken at $(V_{TG}, V_{BG}) = (10, -9\ V)$, and at $T = 3K$.

SIGNATURES OF LINEARLY POLARIZED 1D EXCITONS

We investigate the influence of the 1D confinement potential on the polarization of localized states by performing reflection measurements using linearly co-polarized excitation and detection. In monolayer TMDs, K^+ and K^- valleys excitons can be selectively probed using σ^+/σ^- light[37–39]. However, we expect the 1D excitonic confinement to perturb the valley

circular dichroism. At the edge of the top gate finger, we record polarization-resolved differential reflection spectra, as shown in Fig. 2a–d. Each localized state is linearly polarized, and we find two groups (LS_1^L ; LS_3^L) and $\left(\{LS_1^U; LS_2^L\}\ ;\ LS_2^U\right)$, which are co-polarized either parallel (∥) or perpendicular (⊥) to the electrode's edge, respectively. The degree of polarization of the second state (ie. $\{LS_1^U; LS_2^L\}$) is less pronounced and is discussed in the next section. These results imply that excitons near the top gate edge cannot be described in the circular-polarization-accessible base of K and K′ valley but rather as a linear combination of both valleys – accessible via a pair of linearly polarized perpendicular light vectors. Such pairs of cross-polarized excitons have been reported on similar TMD monolayers.[25,40]

To track the polarization characteristics of the states along the edge of the top gate, we acquire hyperspectral reflectance maps with a fixed linear polarization shown in Fig. 2e. We observe distinct spectral weight patterns for the localized states, as depicted in Fig. 2e-h. Here, LS_1^L and LS_3^L follow the vertical edges of the top gate's fingertips while $\{LS_1^U; LS_2^L\}$ and LS_2^U emerge prominently along the longer edges of the fingers. These findings suggest that LS_1^L and LS_3^L exhibit parallel (∥) polarization with respect to the top gate edge, while $\{LS_1^U; LS_2^L\}$ and LS_2^U display perpendicular (⊥) polarization. Our study showcases the role of the top-gate electrode geometry in producing a strongly polarized 1D potential featuring localized excitonic states. Subsequently, we examine the underlying mechanism for generating cross-polarized pairs of localized excitons.

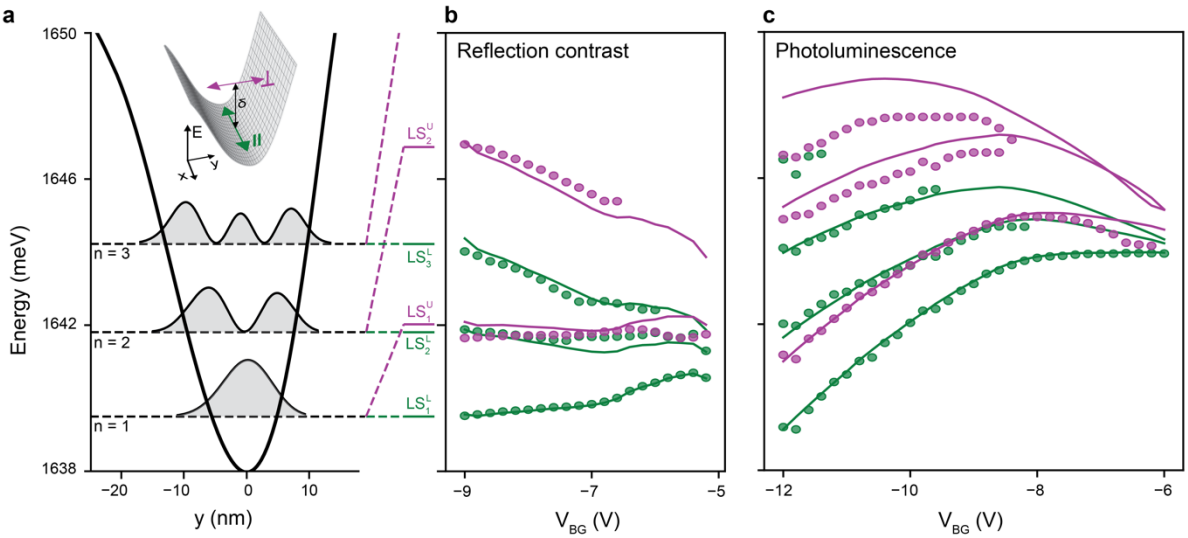

Figure 3: Enhanced valley exchange interaction in 1D trapping potential. a: Simulated confinement potential using Eq. 1, showing quantized levels that coincide with the fitted results of the reflection data at $V_{BG} = -9\ V$. Such confined excitons show fine structure splitting, with lower/upper branches (green and purple dashed lines, respectively). These states are linearly polarized, respectively aligned either parallel ∥ or perpendicular ⊥ to the channel axis (inset). **b-c**: By adapting the exchange coupling constant γ, simulated (lines) states can be brought in close agreement with fitted energies of the localized states shown for ∥/⊥-polarization (green/purple dots, respectively). All reflection contrast (**b**) and photoluminescence (**c**) measurements taken at $T = 3$ K and $V_{TG} = 10$ V with illumination/collection spot located at the edge of the top gate electrode.

VALLEY-HYBRIDIZATION OF 1D-CONFINED STATES

We have established a clear correlation between the emergence of linearly polarized localized states and the qualitative description of an electrostatic 1D trapping potential. However, the precise formation and fine structure of these states remain elusive. Here, our approach involves simulating the accurate exciton potential near the top-gate edge. Our model considers the device geometry shown in Fig. 1a. By defining the gates' and monolayer

electrochemical potentials and solving the system's non-linear Poisson equation (Supplementary Note 2), we obtain the spatial distribution of charge carrier density n and in-plane electric field $\mathcal{E}$. For each input (V_{TG}, V_{BG}), we compute n and $\mathcal{E}$, and extract the exciton potential using Eq. 1. By solving the Hamiltonian of the exciton's center-of-mass motion, we obtain multiple localized state solutions LS_n (with n being the index of the localized state). Every LS_n can be adequately characterized as a standing wave, with an average wavevector denoted as $\bar{k}_n$. Notably, $\bar{k}_n$ lies beyond the boundaries of the light cone, exhibiting values approximately equal to 10 times the light wavevector (q_{light}) (Supplementary Note 5). In practical terms, this implies a substantial transfer of momentum from the trapping potential to the exciton, whereby $\bar{k}_n$ progressively increases as the trapping potential becomes stiffer (cf. Fig. 3a). This renders the exchange-interaction splitting $\delta_n = \gamma\bar{k}_n$ to be larger than the exciton's linewidth. Here, γ is the exchange-interaction coupling parameter governed by long-range exchange interaction[41,42]. The resulting fine structure splitting, splits each LS_n into a lower branch LS_n^L ∥-polarized and an upper branch LS_n^U ⊥-polarized (inset Fig. 3a) with:

$$E_n^{U/L} = E_n + \frac{\delta_n}{2}(1 \pm 1). \qquad \text{Eq. 2}$$

To resolve δ_n, we record RC and PL spectra as a function of V_{BG} under linear ∥/⊥ polarizations, as shown in Fig. 3b-c. Lower branches LS_n^L can be resolved under ∥-polarization and give direct information about the trapping potential's energy levels as by definition $E_n^L = E_n$. To match simulated energy levels to this data, we set exciton masses to $m_{eff} = 1.3\ (1.1)\ m^*$ in RC (PL). On the other hand, upper branches LS_n^U can be resolved under ⊥-polarization, and the exchange-interaction splitting is obtained from $\delta_n = E_n^U - E_n^L$. We show an agreement with the simulations for all energy levels over a large gate voltage range by matching a single constant coupling parameter $\gamma = 14\ (22)\ meV \cdot nm$ in RC (PL). Interestingly, γ is linked to the radiative decay rate through expression[41] $\Gamma_{rad} = n_{hBN}E_n/(\hbar^2 c) \cdot \gamma$ with hBN refractive

index n_{hBN}. This yields $\Gamma_{rad} = [0.39 - 0.61]\ ps^{-1}$ for $n_{hBN} = 2.18$ ([43]). Here, the trapping potential seems to slightly decrease recombination rates in comparison to the unbound exciton recombination rate of $\Gamma_0 \sim 3 \cdot ps^{-1}$, likely due to the in-plane electric field increasing electron-hole separation. Furthermore, the unbound exciton's Fourier limited linewidth sets a lower bound of $FWHM_{X_0} \geq \Gamma_0 \hbar/2 = 1.10$ meV, while $FWHM_{LS} \geq [0.13 - 0.20]$ meV – consistent with the measured localized state linewidth as low as 0.5 meV. This combined analysis of gate-dependent measurements and simulations reveals that the previously identified LS_b state consists of overlapping LS_1^U ($\perp$) and LS_2^L ($\parallel$) states. This observation demonstrates the presence of linearly polarized states $LS_{a,c,d}$ and partially polarized LS_b, which aligns with the data shown in the previous section (Fig. 2).

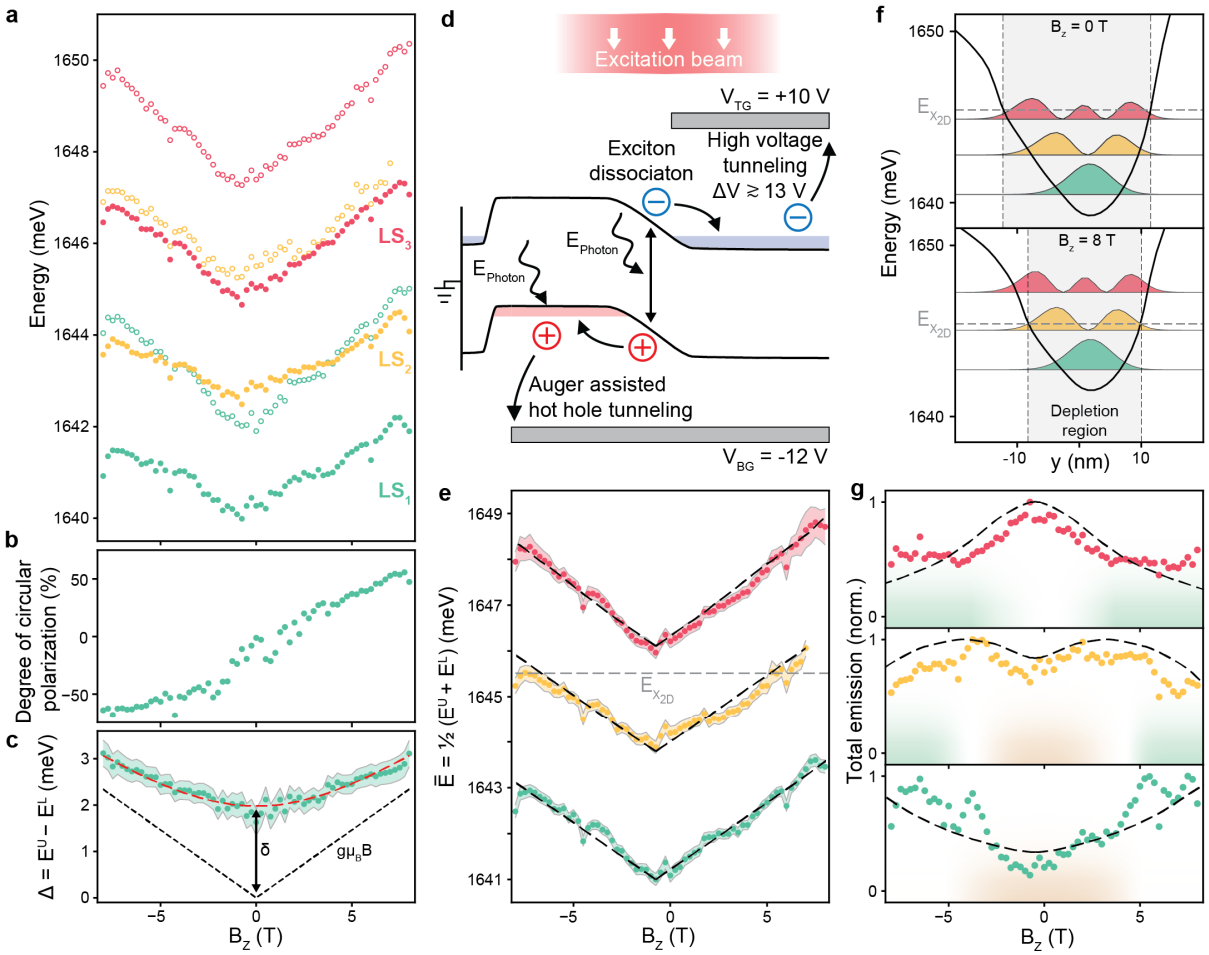

Figure 4: Photoluminescence of quantum-confined 1D exciton under out-of-plane magnetic field. a: Localized state energy as a function of out-of-plane magnetic field B_Z. For the three localized states identified by different colors, upper (circles) and lower (filled circles) branch energies $E^{U/L}$ are extracted. This data is compiled from four measurements under different detection polarizations ($\|$; $\perp$; σ^+; σ^-) (Supplementary Note 6). In each of these measurements the excitation is σ^+ polarized. **b**: Degree of circular polarization as a function of B_z for LS_1^L extracted from polarized PL measurements (other states shown in Supplementary Note 6). **c**: Fine structure splitting $\Delta_1 = E_1^U - E_1^L$ as a function of the magnetic field and fitted data using Eq. 3 (red dashed line). **d**: Schematic band diagram at the top gate edge under illumination. Exact doping is given by the equilibrium between exciton dissociation and Auger assisted hot hole tunneling to the bottom-gate electrode. **e**: Average energies of $LS_{1,2,3}$ as a function of B_z. For each value of the magnetic field, we assign a charge carrier distribution and compute trapping potential as well as localized states energies (dashed lines) or wavefunctions (see cases for $B_z = 0; 8\ T$ shown in **f**). **g**: Total emission intensity for each localized state $LS_{1,2,3}$ as a function of B_z. Normalized exciton population (dashed lines) is calculated taking into account different decay channels associated to exciton dissociation (orange shading) and polaron-exciton interactions (green shading). All measurements are taken at $(V_{TG};\ V_{BG}) = (10;\ -12\ V)$ and $T = 3\ K$ with laser spot located at the edge of the top gate electrode.

MAGNETIC MODULATION OF TRAPPING POTENTIAL

While magneto-optics typically provide insights into the inner structure of the exciton, an out-of-plane magnetic field B_z can also locally affect the electrostatic environment. Solving the B_z-dependent Hamiltonian of the localized exciton, we obtain a new expression of Eq. 2 for the upper (U) and lower (L) states energies:

$$E_n^{U/L} = E_n^X + \frac{\delta_n}{2} + E_{dia} \pm \frac{1}{2}\sqrt{\delta_n^2 + (g_n \mu_B B_z)^2} \qquad \text{Eq. 3}$$

where $E_{dia} = e^2\langle r_n^2\rangle B_z^2/(8\mu)$ is the diamagnetic shift with $\langle r^2\rangle$ being the confined exciton root-mean-square (rms) size, and μ the exciton reduced effective mass. The Zeeman shift is $g_n \mu_B B_z$, where g_n is the g-factor for localized exciton and μ_B is the Bohr magneton. In Fig. 4a, we show polarization-resolved PL measurements of localized states as a function of B_z. While the localized states are linearly polarized at $B_z = 0$ T (see Fig. 2), they become circularly polarized for $|B_z| > 0$. This effect is clear for the lower branch of LS_1^L, as shown in Fig. 4b, and is consistent with an increased lifting of valley degeneracy with B_z (Supplementary Note 6). The fine structure splitting $\Delta_1 = \mathrm{E_1^U} - \mathrm{E_1^L}$ for LS_1 is shown in Fig. 4c. At $B_z = 0$ T, LS_1^L and LS_1^U are energetically separated by the exchange-interaction splitting δ. For large magnetic fields, the Zeeman splitting dominates and the fine structure splitting becomes linear with B_z. Fitting the data with Eq. 3, we obtain $\delta_1 = 2.0$ meV and $g_1 = 5.1$, comparable with delocalized exciton g-factors in encapsulated[44] $MoSe_2$. The diamagnetic shift, typically associated with the exciton internal structure, is captured by the average energy of each localized state, $\bar{E}_n = (\mathrm{E_n^U} + \mathrm{E_n^L})/2 = E_n^X + \delta_n/2 + E_{dia}$, as depicted in Fig. 4e. All localized states exhibit a significant linear shift with the magnetic field (> 230 μeV/T). This finding aligns with the previously reported linear dependence[25] of $\bar{E}_n(B_z)$. It is intriguing because the diamagnetic shift is expected to scale quadratically with B_z, considering that the magnetic length, $l_c = \sqrt{\hbar/eB_z} \sim 26$ nm for $\mathrm{B_z} = 1$ T, is substantially larger than the nanometer scale of the confined exciton[45].

To provide a potential explanation for this behavior, we develop a model based on a dependence of the charge carrier density on the magnetic field, as illustrated in Fig. 4d. This charge carrier density then modifies the electrostatic trapping potential. Through such doping

configuration, both the n-doped region under the top gate and the whole bottom-gated p-doped region are isolated from the electrical ground by depletion regions. This prevents a direct control of the charge carrier density by the gate electrodes. We identify exciton dissociation at the illuminated top gate edge as an effective doping mechanism. The exact charge carrier distribution is then given by an equilibrium between dissociation and tunneling to the gate electrodes via electron tunneling[46] and Auger-assisted hot hole tunneling[47]. While additional charge carriers from exciton dissociation accumulate in p- and n-doped regions, this accumulation is compensated by tunneling events from the doped regions towards the gate electrodes. Interestingly, both exciton dissociation and Auger-assisted tunneling rates scale linearly with the illumination fluence, minimizing the impact of variation in laser power on the measurements (data shown in Supplementary 7). In the latter case, holes from K^+/K^- valleys gain energy through Auger recombination. At such elevated energies, z-components of bands at the Γ point hybridize with hBN bands, facilitating hole tunneling to the bottom-gate electrode. This process requires $K \rightarrow \Gamma$ phonon-assisted scattering. With increasing magnetic field, the valence bands at K^+/K^- may become more resilient to spin-depolarizing scattering events[48], thereby reducing the Auger tunneling rate.

To model this phenomenon, we simulate the trapping potential as a function of the charge carrier density in the p-doped region while maintaining $(V_{TG};\, V_{BG}) = (10;\, -12\,\mathrm{V})$ (as described in Supplementary Note 2). The charge carrier density $n(B_z)$ is extracted by fitting the lowest state energy $\bar{E}_1(B_z)$, as shown in Fig. 4e-f. In this model, we implicitly hypothesize that the magnetic field induces modifications in the distribution of charge carriers by up to $\Delta n(0 \rightarrow 8\mathrm{T}) \sim 0.22\,.\,10^{12}\ \mathrm{cm}^{-2}$, consequently altering the trapping potential. Experimental evidence supporting this model includes three independent observations. First, the measured photocurrent, corresponding to the tunneling towards the bottom-gate electrode, decreases by 25% when the magnetic field is switched to $B_z = 8\ \mathrm{T}$ (data shown in Supplementary Note 8).

Second, the linear dependence of the average energy $\bar{E}_n(B_z)$ of the confined states is accurately fitted by our model, as shown in Fig. 4e. This agreement additionally resolves the discrepancy discussed in ref., between a considerable rms size of the localized exciton, extracted from a hypothetical diamagnetic shift ($\Delta\bar{E}_n \sim 2$ meV at 8 T), and the observed significant oscillator strength in RC measurements (cf. Fig 1e). The final evidence pertains to the change in total emission intensity, depicted in Fig. 4g. As the emission polarization changes with B_z, it is necessary to extract the total emission intensity, also known as the S_0 Stokes parameter, for each localized state (Supplementary Note 6). This enables us to distinguish intensity variations caused by the polarizers from the inherent decay of the exciton population and shows that the total emission of $LS_{1,2,3}$ varies with B_z. Specifically, as B_z increases, the intensity of LS_1 decreases, displaying an opposite trend to that of LS_3. LS_2 is an intermediate situation, with a slight intensity increase at low magnetic fields and a reduction at larger values.

This behavior can be explained by the magnetic-field-dependent charge carrier distribution, which affects the strength of Stark and interaction confinement for each localized state (Supplementary Note 9). For instance, localized states like LS_1, which have lower energy than the unconfined exciton X_{2D} (indicated by the dashed line in Fig. 4e), are primarily confined by the Stark effect (orange shading in Fig. 4g). On the other hand, higher energy states like LS_3 are strongly influenced by the interaction shift (green shading in Fig. 4g) as their wavefunction extends into regions with higher doping. The in-plane electric field decreases at higher magnetic fields, resulting in reduced exciton dissociation, thereby naturally increasing the LS_1 intensity. In contrast, LS_3 is more affected by the exciton-polaron interaction shift than Stark confinement. The polaron coupling is enhanced at larger B_z values, creating a non-radiative decay channel that decreases emission intensity for LS_3. Our model is built upon the influence of an out-of-plane magnetic field, which alters the distribution of charge carriers in $MoSe_2$ near the top-gate edge. The precise underlying mechanism can be attributed to reduced spin-

depolarizing scattering events[48] within the valence bands at K^+/K^- points. This reduction leads to a decrease in the rate of Auger tunneling as the magnitude of the magnetic field is increased. This model could be further tested with time-resolved valley polarization measurements.

CONCLUSIONS

In this study, we first replicated electrostatically quantum-confined intra-layer excitons in 1D channels, as recently demonstrated. We then observed and modeled the hybridization between oppositely polarized states in confined regions. Additionally, we provided experimental evidence and a model to understand the unique magneto-optic response of the 1D confined states. Three key aspects are highlighted in this study: first, a large inhomogeneous in-plane electric field enables quantum confinement of neutral excitons. The spatial extent of the localization potential is not limited by lithographic resolution, suggesting alternative methods, such as exploiting ferroelectric material grain boundaries[30]. In addition, confining intra-layer excitons offers enhanced light-matter interactions and the possibility of coupling to nanophotonic architectures, compared to inter-layer exciton manipulation. Furthermore, electrical tuning of confined state position at the nanometer scale offers a degree of control to study dipolar interactions[2]. Second, gate-tunable valley hybridization facilitates electrically addressable 2D devices exploiting in situ tunable chiral light-matter interactions that can be further enhanced using the efficient coupling of 2D heterostructures with metasurfaces[49], for instance. Finally, the geometry of the top electrode dictates the 1D confinement potential, which can be further engineered[50] to create 0D structures[26,27,31] and periodic arrays made of quantum emitters[13] or valley-selective quantum emitters[51]. These configurations are promising for investigating quantum-collective effects and their applications in emergent quantum technologies, including quantum simulation[51], sensor arrays[52], and photon storage[53].

MATERIALS AND METHODS

Reflectance contract (RC) measurements are performed in a confocal microscope setup with 0.7 NA (100X Mitutoyo Plan Apo NIR HR) and a closed-cycle cryostat (Montana Cryostation). For excitation, we use a supercontinuum laser source combined with a variable wavelength filter with a 6 nm spectral window (SuperK Extreme) with typical power of 10 nW and spot size ~750 nm. During RC measurements, no other light sources are switched on. The polarization is controlled by a single linear polarizer on an automated rotation stage in front of the objective.

Micro-photoluminescence (μ-PL) measurements are performed in a confocal (SM/SM) microscope setup with 0.81 NA (Attocube LT-APO/NIR/0.81) within a closed-cycle cryostat (Attocube AttoDRY1000). We use a 660 nm cw-laser source (Laser Quantum Ventus 660) with 2 μW power and ~550 nm spot-size for excitation. Excitation and detection polarization are separately controlled by units of $\lambda/2$ and $\lambda/4$, each on automated rotation stages. Both setups use XYZ scanning stages.

Device preparation: layers (exfoliated $MoSe_2$, hBN, graphite) are picked up with a polypropylene-carbonate (PPC) coated PDMS stamp at 100°C for the hBN and graphite and room temperature for the TMD. The complete stack is dropped on a Si/SiO_2 (285nm) chip with pre-patterned electrodes for the bottom-gate and TMD, which is contacted with a few layers graphite flake. The release is done at 180°C, and the residual film is removed in chloroform and isopropanol. Lastly, the top gate is patterned directly on the stack by electron beam lithography and thin film evaporation deposition. All the contacts are made of 2nm Ti layer and an Au layer of 15nm for the pre-patterned electrodes, and 10nm for the top gate.

ASSOCIATED CONTENT

A previous version of this work[54] can be found on a preprint server.

(Word Style "TE_Supporting_Information"). **Supporting Information**.

Please find below additional experimental and analysis details related to our research. This includes a detailed description of the sample geometry, observation of localized states in opposite NP configuration, electrostatic simulation of exciton trapping potential, determination of the valley exchange coupling, details on magneto-optics measurements, photocurrent measurements, illumination power dependence, and exciton decay rates vs. magnetic field. A PDF file containing this information is available free of charge.

AUTHOR INFORMATION

Corresponding Author

* Corresponding authors: antoine.reserbat-plantey@cnrs.fr, frank.koppens@icfo.eu

Author Contributions

Manuscript was written through contributions of all authors. All authors have given approval to the final version of the manuscript.

ACKNOWLEDGMENT

The authors thank Evgeny Alexeev, François Dubin, and Andreas Stier for constructive discussions and Matteo Ceccanti for his advice and help in the sample gates fabrication. F.H.L.K.

acknowledges support from the ERC TOPONANOP (726001), PCI2021-122020-2A funded by MCIN/AEI/ 10.13039/501100011033), the "European Union NextGenerationEU/PRTR (PRTR-C17.I1), D.E.C acknowledges support from the European Union, under European Research Council grant agreement No 101002107 (NEWSPIN). F.H.L.K and D.E.C acknowledge support from the government of Spain (PID2019-106875GB-I00; Severo Ochoa CEX2019-000910-S [MCIN/ AEI/10.13039/501100011033], Fundació Cellex, Fundació Mir-Puig, and Generalitat de Catalunya (CERCA, AGAUR, 2021 SGR 01443). Authors thank European Union's Horizon 2020 under grant agreement no. 881603 (Graphene flagship Core3) and 820378 (Quantum flagship). A.R-P thanks support from UCAJEDI ANR-15-IDEX-01, ANR JCJC NEAR-2D (23-CE47-0015) and Doeblin FR 2800. G. C. thanks European Union Horizon 2020 research and innovation programme under the Marie Sklodowska-Curie grant agreement No 882536 (QUANLUX) and QUANTERA 2021 (T-NiSQ). M.S.G.F. thanks EPSRC Doctoral Training Programme. C.M.P. thanks ERC Advanced Grant PEDESTAL (884745). K.W. and T.T. acknowledge support from the JSPS KAKENHI (Grant Numbers 21H05233 and 23H02052) and World Premier International Research Center Initiative (WPI), MEXT, Japan. S.T acknowledges support from DOE-SC0020653, NSF CMMI 1825594, NSF ECCS 2052527, DMR 2111812 and CMMI 2129412.

REFERENCES

(1) Baek, H.; Brotons-Gisbert, M.; Koong, Z. X.; Campbell, A.; Rambach, M.; Watanabe, K.; Taniguchi, T.; Gerardot, B. D. Highly Energy-Tunable Quantum Light from Moiré-Trapped Excitons. *Sci. Adv.* **2020**, *6* (37), eaba8526. https://doi.org/10.1126/sciadv.aba8526.

(2) Li, W.; Lu, X.; Dubey, S.; Devenica, L.; Srivastava, A. Dipolar Interactions between Localized Interlayer Excitons in van Der Waals Heterostructures. *Nat. Mater.* **2020**, *19* (6), 624–629. https://doi.org/10.1038/s41563-020-0661-4.

(3) Unuchek, D.; Ciarrocchi, A.; Avsar, A.; Watanabe, K.; Taniguchi, T.; Kis, A. Room-Temperature Electrical Control of Exciton Flux in a van Der Waals Heterostructure. *Nature* **2018**, *560* (7718), 340–344. https://doi.org/10.1038/s41586-018-0357-y.

(4) Regan, E. C.; Wang, D.; Jin, C.; Bakti Utama, M. I.; Gao, B.; Wei, X.; Zhao, S.; Zhao, W.; Zhang, Z.; Yumigeta, K.; Blei, M.; Carlström, J. D.; Watanabe, K.; Taniguchi, T.; Tongay, S.; Crommie, M.; Zettl, A.; Wang, F. Mott and Generalized Wigner Crystal States in WSe_2/WS_2 Moiré Superlattices. *Nature* **2020**, *579* (7799), 359–363. https://doi.org/10.1038/s41586-020-2092-4.
(5) Smoleński, T.; Dolgirev, P. E.; Kuhlenkamp, C.; Popert, A.; Shimazaki, Y.; Back, P.; Lu, X.; Kroner, M.; Watanabe, K.; Taniguchi, T.; Esterlis, I.; Demler, E.; Imamoğlu, A. Signatures of Wigner Crystal of Electrons in a Monolayer Semiconductor. *Nature* **2021**, *595* (7865), 53–57. https://doi.org/10.1038/s41586-021-03590-4.
(6) Palacios-Berraquero, C.; Kara, D. M.; Montblanch, A. R.-P.; Barbone, M.; Latawiec, P.; Yoon, D.; Ott, A. K.; Loncar, M.; Ferrari, A. C.; Atatüre, M. Large-Scale Quantum-Emitter Arrays in Atomically Thin Semiconductors. *Nat Commun* **2017**, *8* (1), 15093. https://doi.org/10.1038/ncomms15093.
(7) Branny, A.; Kumar, S.; Proux, R.; Gerardot, B. D. Deterministic Strain-Induced Arrays of Quantum Emitters in a Two-Dimensional Semiconductor. *Nat Commun* **2017**, *8* (1), 15053. https://doi.org/10.1038/ncomms15053.
(8) Massicotte, M.; Vialla, F.; Schmidt, P.; Lundeberg, M. B.; Latini, S.; Haastrup, S.; Danovich, M.; Davydovskaya, D.; Watanabe, K.; Taniguchi, T.; Fal'ko, V. I.; Thygesen, K. S.; Pedersen, T. G.; Koppens, F. H. L. Dissociation of Two-Dimensional Excitons in Monolayer WSe_2. *Nat Commun* **2018**, *9* (1), 1633. https://doi.org/10.1038/s41467-018-03864-y.
(9) Baugher, B. W. H.; Churchill, H. O. H.; Yang, Y.; Jarillo-Herrero, P. Optoelectronic Devices Based on Electrically Tunable p–n Diodes in a Monolayer Dichalcogenide. *Nature Nanotech* **2014**, *9* (4), 262–267. https://doi.org/10.1038/nnano.2014.25.
(10) Ishii, H.; Kataura, H.; Shiozawa, H.; Yoshioka, H.; Otsubo, H.; Takayama, Y.; Miyahara, T.; Suzuki, S.; Achiba, Y.; Nakatake, M.; Narimura, T.; Higashiguchi, M.; Shimada, K.; Namatame, H.; Taniguchi, M. Direct Observation of Tomonaga–Luttinger-Liquid State in Carbon Nanotubes at Low Temperatures. *Nature* **2003**, *426* (6966), 540–544. https://doi.org/10.1038/nature02074.
(11) Stampfer, C.; Schurtenberger, E.; Molitor, F.; Güttinger, J.; Ihn, T.; Ensslin, K. Tunable Graphene Single Electron Transistor. *Nano Lett.* **2008**, *8* (8), 2378–2383. https://doi.org/10.1021/nl801225h.
(12) Cepellotti, A.; Fugallo, G.; Paulatto, L.; Lazzeri, M.; Mauri, F.; Marzari, N. Phonon Hydrodynamics in Two-Dimensional Materials. *Nat Commun* **2015**, *6* (1), 6400. https://doi.org/10.1038/ncomms7400.
(13) Hu, Q.; Zhan, Z.; Cui, H.; Zhang, Y.; Jin, F.; Zhao, X.; Zhang, M.; Wang, Z.; Zhang, Q.; Watanabe, K.; Taniguchi, T.; Cao, X.; Liu, W.-M.; Wu, F.; Yuan, S.; Xu, Y. Observation of Rydberg Moiré Excitons. *Science* **2023**, *380* (6652), 1367–1372. https://doi.org/10.1126/science.adh1506.
(14) Azzam, S. I.; Parto, K.; Moody, G. Prospects and Challenges of Quantum Emitters in 2D Materials. *Appl. Phys. Lett.* **2021**, *118* (24), 240502. https://doi.org/10.1063/5.0054116.
(15) Klein, J.; Lorke, M.; Florian, M.; Sigger, F.; Sigl, L.; Rey, S.; Wierzbowski, J.; Cerne, J.; Müller, K.; Mitterreiter, E.; Zimmermann, P.; Taniguchi, T.; Watanabe, K.; Wurstbauer, U.; Kaniber, M.; Knap, M.; Schmidt, R.; Finley, J. J.; Holleitner, A. W. Site-Selectively Generated Photon Emitters in Monolayer MoS_2 via Local Helium Ion Irradiation. *Nat Commun* **2019**, *10* (1), 2755. https://doi.org/10.1038/s41467-019-10632-z.

(16) Seyler, K. L.; Rivera, P.; Yu, H.; Wilson, N. P.; Ray, E. L.; Mandrus, D. G.; Yan, J.; Yao, W.; Xu, X. Signatures of Moiré-Trapped Valley Excitons in $MoSe_2/WSe_2$ Heterobilayers. *Nature* **2019**, *567* (7746), 66–70. https://doi.org/10.1038/s41586-019-0957-1.
(17) Montblanch, A. R.-P.; Barbone, M.; Aharonovich, I.; Atatüre, M.; Ferrari, A. C. Layered Materials as a Platform for Quantum Technologies. *Nat. Nanotechnol.* **2023**, *18* (6), 555–571. https://doi.org/10.1038/s41565-023-01354-x.
(18) Vögele, X. P.; Schuh, D.; Wegscheider, W.; Kotthaus, J. P.; Holleitner, A. W. Density Enhanced Diffusion of Dipolar Excitons within a One-Dimensional Channel. *Phys. Rev. Lett.* **2009**, *103* (12), 126402. https://doi.org/10.1103/PhysRevLett.103.126402.
(19) Chakraborty, C.; Goodfellow, K. M.; Dhara, S.; Yoshimura, A.; Meunier, V.; Vamivakas, A. N. Quantum-Confined Stark Effect of Individual Defects in a van Der Waals Heterostructure. *Nano Lett.* **2017**, *17* (4), 2253–2258. https://doi.org/10.1021/acs.nanolett.6b04889.
(20) Vialla, F.; Danovich, M.; Ruiz-Tijerina, D. A.; Massicotte, M.; Schmidt, P.; Taniguchi, T.; Watanabe, K.; Hunt, R. J.; Szyniszewski, M.; Drummond, N. D.; Pedersen, T. G.; Fal'ko, V. I.; Koppens, F. H. L. Tuning of Impurity-Bound Interlayer Complexes in a van Der Waals Heterobilayer. *2D Mater.* **2019**, *6* (3), 035032. https://doi.org/10.1088/2053-1583/ab168d.
(21) Jauregui, L. A.; Joe, A. Y.; Pistunova, K.; Wild, D. S.; High, A. A.; Zhou, Y.; Scuri, G.; De Greve, K.; Sushko, A.; Yu, C.-H.; Taniguchi, T.; Watanabe, K.; Needleman, D. J.; Lukin, M. D.; Park, H.; Kim, P. Electrical Control of Interlayer Exciton Dynamics in Atomically Thin Heterostructures. *Science* **2019**, *366* (6467), 870–875. https://doi.org/10.1126/science.aaw4194.
(22) Liu, Y.; Dini, K.; Tan, Q.; Liew, T.; Novoselov, K. S.; Gao, W. Electrically Controllable Router of Interlayer Excitons. *Sci. Adv.* **2020**, *6* (41), eaba1830. https://doi.org/10.1126/sciadv.aba1830.
(23) Zhao, S.; Li, Z.; Huang, X.; Rupp, A.; Göser, J.; Vovk, I. A.; Kruchinin, S. Y.; Watanabe, K.; Taniguchi, T.; Bilgin, I.; Baimuratov, A. S.; Högele, A. Excitons in Mesoscopically Reconstructed Moiré Heterostructures. *Nat. Nanotechnol.* **2023**, *18* (6), 572–579. https://doi.org/10.1038/s41565-023-01356-9.
(24) Raja, A.; Chaves, A.; Yu, J.; Arefe, G.; Hill, H. M.; Rigosi, A. F.; Berkelbach, T. C.; Nagler, P.; Schüller, C.; Korn, T.; Nuckolls, C.; Hone, J.; Brus, L. E.; Heinz, T. F.; Reichman, D. R.; Chernikov, A. Coulomb Engineering of the Bandgap and Excitons in Two-Dimensional Materials. *Nat Commun* **2017**, *8* (1), 15251. https://doi.org/10.1038/ncomms15251.
(25) Thureja, D.; Imamoglu, A.; Smoleński, T.; Amelio, I.; Popert, A.; Chervy, T.; Lu, X.; Liu, S.; Barmak, K.; Watanabe, K.; Taniguchi, T.; Norris, D. J.; Kroner, M.; Murthy, P. A. Electrically Tunable Quantum Confinement of Neutral Excitons. *Nature* **2022**, *606* (7913), 298–304. https://doi.org/10.1038/s41586-022-04634-z.
(26) Thureja, D.; Yazici, F. E.; Smolenski, T.; Kroner, M.; Norris, D. J.; Imamoglu, A. Electrically Defined Quantum Dots for Bosonic Excitons. arXiv March 4, 2024. http://arxiv.org/abs/2402.19278 (accessed 2024-04-04).
(27) Hu, J.; Lorchat, E.; Chen, X.; Watanabe, K.; Taniguchi, T.; Heinz, T. F.; Murthy, P. A.; Chervy, T. Quantum Control of Exciton Wave Functions in 2D Semiconductors. *Sci. Adv.* **2024**, *10* (12), eadk6369. https://doi.org/10.1126/sciadv.adk6369.
(28) Dirnberger, F.; Ziegler, J. D.; Faria Junior, P. E.; Bushati, R.; Taniguchi, T.; Watanabe, K.; Fabian, J.; Bougeard, D.; Chernikov, A.; Menon, V. M. Quasi-1D Exciton Channels in Strain-Engineered 2D Materials. *Science Advances* **2021**, *7* (44). https://doi.org/10.1126/sciadv.abj3066.

(29) Almutlaq, J.; Wang, J.; Li, L.; Li, C.; Dang, T.; Bulović, V.; Kong, J.; Englund, D. Electrical Tuning of Neutral and Charged Excitons with 1-Nm Gate. arXiv October 30, 2023. http://arxiv.org/abs/2310.19895 (accessed 2024-04-05).
(30) Soubelet, P.; Klein, J.; Wierzbowski, J.; Silvioli, R.; Sigger, F.; Stier, A. V.; Gallo, K.; Finley, J. J. Charged Exciton Kinetics in Monolayer $MoSe_2$ near Ferroelectric Domain Walls in Periodically Poled $LiNbO_3$. *Nano Lett.* **2021**, *21* (2), 959–966. https://doi.org/10.1021/acs.nanolett.0c03810.
(31) Moon, H.; Mennel, L.; Chakraborty, C.; Peng, C.; Almutlaq, J.; Taniguchi, T.; Watanabe, K.; Englund, D. Nanoscale Confinement and Control of Excitonic Complexes in a Monolayer WSe2. arXiv November 30, 2023. http://arxiv.org/abs/2311.18660 (accessed 2024-04-05).
(32) Efimkin, D. K.; MacDonald, A. H. Many-Body Theory of Trion Absorption Features in Two-Dimensional Semiconductors. *Phys. Rev. B* **2017**, *95* (3), 035417. https://doi.org/10.1103/PhysRevB.95.035417.
(33) Ossau, W. J.; Suris, R. *Optical Properties of 2D Systems with Interacting Electrons*, Springer Netherlands.; Springer Netherlands: Dordrecht, 2003. https://doi.org/10.1007/978-94-010-0078-9.
(34) Cadiz, F.; Courtade, E.; Robert, C.; Wang, G.; Shen, Y.; Cai, H.; Taniguchi, T.; Watanabe, K.; Carrere, H.; Lagarde, D.; Manca, M.; Amand, T.; Renucci, P.; Tongay, S.; Marie, X.; Urbaszek, B. Excitonic Linewidth Approaching the Homogeneous Limit in MoS_2-Based van Der Waals Heterostructures. *Phys. Rev. X* **2017**, *7* (2), 021026. https://doi.org/10.1103/PhysRevX.7.021026.
(35) Sidler, M.; Back, P.; Cotlet, O.; Srivastava, A.; Fink, T.; Kroner, M.; Demler, E.; Imamoglu, A. Fermi Polaron-Polaritons in Charge-Tunable Atomically Thin Semiconductors. *Nature Phys* **2017**, *13* (3), 255–261. https://doi.org/10.1038/nphys3949.
(36) Liu, E.; van Baren, J.; Lu, Z.; Taniguchi, T.; Watanabe, K.; Smirnov, D.; Chang, Y.-C.; Lui, C. H. Exciton-Polaron Rydberg States in Monolayer $MoSe_2$ and WSe_2. *Nat Commun* **2021**, *12* (1), 6131. https://doi.org/10.1038/s41467-021-26304-w.
(37) Wang, G.; Chernikov, A.; Glazov, M. M.; Heinz, T. F.; Marie, X.; Amand, T.; Urbaszek, B. *Colloquium* : Excitons in Atomically Thin Transition Metal Dichalcogenides. *Rev. Mod. Phys.* **2018**, *90* (2), 021001. https://doi.org/10.1103/RevModPhys.90.021001.
(38) Cao, T.; Wang, G.; Han, W.; Ye, H.; Zhu, C.; Shi, J.; Niu, Q.; Tan, P.; Wang, E.; Liu, B.; Feng, J. Valley-Selective Circular Dichroism of Monolayer Molybdenum Disulphide. *Nat Commun* **2012**, *3* (1), 887. https://doi.org/10.1038/ncomms1882.
(39) Mak, K. F.; He, K.; Shan, J.; Heinz, T. F. Control of Valley Polarization in Monolayer MoS_2 by Optical Helicity. *Nature Nanotech* **2012**, *7* (8), 494–498. https://doi.org/10.1038/nnano.2012.96.
(40) Wang, Q.; Maisch, J.; Tang, F.; Zhao, D.; Yang, S.; Joos, R.; Portalupi, S. L.; Michler, P.; Smet, J. H. Highly Polarized Single Photons from Strain-Induced Quasi-1D Localized Excitons in WSe_2. *Nano Lett.* **2021**, *21* (17), 7175–7182. https://doi.org/10.1021/acs.nanolett.1c01927.
(41) Glazov, M. M.; Ivchenko, E. L.; Wang, G.; Amand, T.; Marie, X.; Urbaszek, B.; Liu, B. L. Spin and Valley Dynamics of Excitons in Transition Metal Dichalcogenide Monolayers. *Physica Status Solidi (b)* **2015**, *252* (11), 2349–2362. https://doi.org/10.1002/pssb.201552211.
(42) Peng, G.-H.; Sanchez, O. J. G.; Li, W.-H.; Lo, P.-Y.; Cheng, S.-J. Tailoring the Superposition of Finite-Momentum Valley Exciton States in Transition-Metal Dichalcogenide Monolayers

by Using Polarized Twisted Light. *Phys. Rev. B* **2022**, *106* (15), 155304. https://doi.org/10.1103/PhysRevB.106.155304.
(43) Lee, S.-Y.; Jeong, T.-Y.; Jung, S.; Yee, K.-J. Refractive Index Dispersion of Hexagonal Boron Nitride in the Visible and Near-Infrared. *Physica Status Solidi (b)* **2019**, *256* (6), 1800417. https://doi.org/10.1002/pssb.201800417.
(44) Goryca, M.; Li, J.; Stier, A. V.; Taniguchi, T.; Watanabe, K.; Courtade, E.; Shree, S.; Robert, C.; Urbaszek, B.; Marie, X.; Crooker, S. A. Revealing Exciton Masses and Dielectric Properties of Monolayer Semiconductors with High Magnetic Fields. *Nat Commun* **2019**, *10* (1), 4172. https://doi.org/10.1038/s41467-019-12180-y.
(45) Maes, J.; Hayne, M.; Sidor, Y.; Partoens, B.; Peeters, F. M.; González, Y.; González, L.; Fuster, D.; García, J. M.; Moshchalkov, V. V. Electron Wave-Function Spillover in Self-Assembled InAs/InP Quantum Wires. *Phys. Rev. B* **2004**, *70* (15), 155311. https://doi.org/10.1103/PhysRevB.70.155311.
(46) Britnell, L.; Gorbachev, R. V.; Jalil, R.; Belle, B. D.; Schedin, F.; Katsnelson, M. I.; Eaves, L.; Morozov, S. V.; Mayorov, A. S.; Peres, N. M. R.; Castro Neto, A. H.; Leist, J.; Geim, A. K.; Ponomarenko, L. A.; Novoselov, K. S. Electron Tunneling through Ultrathin Boron Nitride Crystalline Barriers. *Nano Lett.* **2012**, *12* (3), 1707–1710. https://doi.org/10.1021/nl3002205.
(47) Sushko, A.; De Greve, K.; Phillips, M.; Urbaszek, B.; Joe, A. Y.; Watanabe, K.; Taniguchi, T.; Efros, A. L.; Hellberg, C. S.; Park, H.; Kim, P.; Lukin, M. D. Asymmetric Photoelectric Effect: Auger-Assisted Hot Hole Photocurrents in Transition Metal Dichalcogenides. *Nanophotonics* **2020**, *10* (1), 105–113. https://doi.org/10.1515/nanoph-2020-0397.
(48) Yang, M.; Robert, C.; Lu, Z.; Van Tuan, D.; Smirnov, D.; Marie, X.; Dery, H. Exciton Valley Depolarization in Monolayer Transition-Metal Dichalcogenides. *Phys. Rev. B* **2020**, *101* (11), 115307. https://doi.org/10.1103/PhysRevB.101.115307.
(49) Sun, L.; Wang, C.-Y.; Krasnok, A.; Choi, J.; Shi, J.; Gomez-Diaz, J. S.; Zepeda, A.; Gwo, S.; Shih, C.-K.; Alù, A.; Li, X. Separation of Valley Excitons in a MoS_2 Monolayer Using a Subwavelength Asymmetric Groove Array. *Nature Photon* **2019**, *13* (3), 180–184. https://doi.org/10.1038/s41566-019-0348-z.
(50) Cohen, L. A.; Samuelson, N. L.; Wang, T.; Klocke, K.; Reeves, C. C.; Taniguchi, T.; Watanabe, K.; Vijay, S.; Zaletel, M. P.; Young, A. F. Nanoscale Electrostatic Control in Ultraclean van Der Waals Heterostructures by Local Anodic Oxidation of Graphite Gates. *Nat. Phys.* **2023**, 1–7. https://doi.org/10.1038/s41567-023-02114-3.
(51) Yu, H.; Liu, G.-B.; Tang, J.; Xu, X.; Yao, W. Moiré Excitons: From Programmable Quantum Emitter Arrays to Spin-Orbit–Coupled Artificial Lattices. *Science Advances* **2017**, *3* (11), e1701696. https://doi.org/10.1126/sciadv.1701696.
(52) Tetienne, J.-P.; Dontschuk, N.; Broadway, D. A.; Stacey, A.; Simpson, D. A.; Hollenberg, L. C. L. Quantum Imaging of Current Flow in Graphene. *Sci. Adv.* **2017**, *3* (4), e1602429. https://doi.org/10.1126/sciadv.1602429.
(53) Asenjo-Garcia, A.; Moreno-Cardoner, M.; Albrecht, A.; Kimble, H. J.; Chang, D. E. Exponential Improvement in Photon Storage Fidelities Using Subradiance and "Selective Radiance" in Atomic Arrays. *Phys. Rev. X* **2017**, *7* (3), 031024. https://doi.org/10.1103/PhysRevX.7.031024.
(54) Heithoff, M.; Moreno, Á.; Torre, I.; Feuer, M. S. G.; Purser, C. M.; Andolina, G. M.; Calajo, G.; Watanabe, K.; Taniguchi, T.; Kara, D.; Hays, P.; Tongay, S.; Falko, V.; Chang, D.; Atatüre, M.; Reserbat-Plantey, A.; Koppens, F. Valley-Hybridized Gate-Tunable 1D Exciton

Confinement in MoSe2. arXiv November 15, 2023. http://arxiv.org/abs/2311.05299 (accessed 2024-09-30).